ACS APPLIED MATERIALS & INTERFACES

www.acsami.org Research Article

Competing Energy Transfer in Two-Dimensional Mn^{2+}-Doped $BDACdBr_4$ Hybrid Layered Perovskites with Near-Unity Photoluminescence Quantum Yield

Canxu Chen, Shuai Zhang, Ruosheng Zeng,* Binbin Luo, Yuanjie Chen, Sheng Cao, Jialong Zhao, Bingsuo Zou, and Jin Zhong Zhang*

Cite This: *ACS Appl. Mater. Interfaces* 2022, 14, 45725−45733 Read Online

ABSTRACT: Two-dimensional (2D) hybrid layered perovskites (HLPs) have attracted extensive attention due to their excellent optoelectronic properties. Herein, we successfully prepared high-quality Mn-doped $BDACdBr_4$ (BDA = $NH_2(CH_2)_4NH_2$, butylene diammonium) HLP single crystals (SCs). The incorporation of Mn^{2+} ions modulates the electronic band structure of $BDACdBr_4$ perovskites and tailors the energy transfer process of excited states. A near-unity photoluminescence (PL) quantum yield of 96% from the Mn^{2+} emission at 608 nm is achieved. Excitation wavelength-dependent spectroscopic characterizations help to clarify the energy transfer mechanism of Mn-doped $BDACdBr_4$, in which competing PL from the $^3E_g \rightarrow {}^1A_{1g}$ transition of Cd^{2+} and the $^4T_1(G) \rightarrow {}^6A_1(S)$ transition of Mn^{2+} dopants is observed. Temperature-dependent PL spectroscopic characterizations indicate that the efficient energy transfer from $BDACdBr_4$ perovskite host to Mn^{2+} dopants requires thermal activation to overcome a potential barrier. This work provides new insight into the photophysics and optical properties of 2D HLPs, especially the influence of Mn^{2+} doping on competing energy transfer in hybrid luminescent materials.

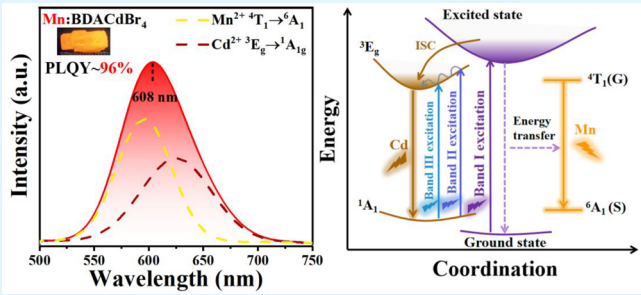

KEYWORDS: *two-dimensional hybrid perovskites, Mn-doped, photoluminescence, energy transfer, excitation wavelength-dependent optical properties, thermal activation*

1. INTRODUCTION

In recent years, two-dimensional (2D) halogenated layered perovskites have attracted extensive attention due to their high photoluminescence (PL) quantum yield (QY), high carrier mobility, long exciton diffusion length, and outstanding stability.[1−5] This class of materials has been used in solar cells,[6−8] light-emitting diodes (LEDs),[9−12] and photodetectors,[13−15] demonstrating excellent optoelectronic performance. More recently, 2D hybrid layered perovskites (HLPs) with covalently bonded metal monolayers have shown tunable electronic and optical properties of interest for various photonic applications.[16,17] The assembly of organic cations can not only expand the diversity of 2D layered perovskites but also modulate the band structure and photophysical properties.[18−20] Therefore, in-depth understanding of the fundamental optoelectronic properties of 2D HLPs is highly desired.[21,22]

2D A_2MX_4 HLPs (A: organic ammonium; M: divalent metal; X: halogen) are composed of organic ammonium chain cation A^+ monolayers altering with inorganic corner-sharing metal halide octahedron $[MX_4]^{2-}$ backbone monolayers, where the adjacent layers are weakly bound through a weak van der Waals force.[23,24] Recently, HLPs with such a layered structure have shown excellent optical properties and device performance.[16] BA_2PbBr_4 (BA = $C_4H_9NH_2$, butylamine) is an example of such HLPs with a large band gap of 3.0 eV. Due to its large band gap, its application in the photovoltaic field is limited. However, it shows great prospects in photodetector applications. For example, the high-performance UV photodetector based on BA_2PbBr_4 perovskite single crystals (SCs) shows extremely low dark current and high stability of multiple-cycle UV response.[25,26] Similarly, 2D $BDACdBr_4$ (BDA = $NH_2(CH_2)_4NH_2$, butylene diammonium) HLPs also demonstrated prominent photoelectric detection performance.[27] The photodetector based on 2D $BDACdBr_4$ perovskite SC exhibits a stable UV−visible photoelectric response. More recently, the optical performance of 2D $BDACdBr_4$ HLPs is greatly improved through Pb^{2+}/Sb^{3+} doping with ns^2 electrons.

Received: August 2, 2022
Accepted: September 23, 2022
Published: October 3, 2022

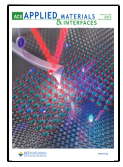

https://doi.org/10.1021/acsami.2c13878
ACS Appl. Mater. Interfaces 2022, 14, 45725−45733

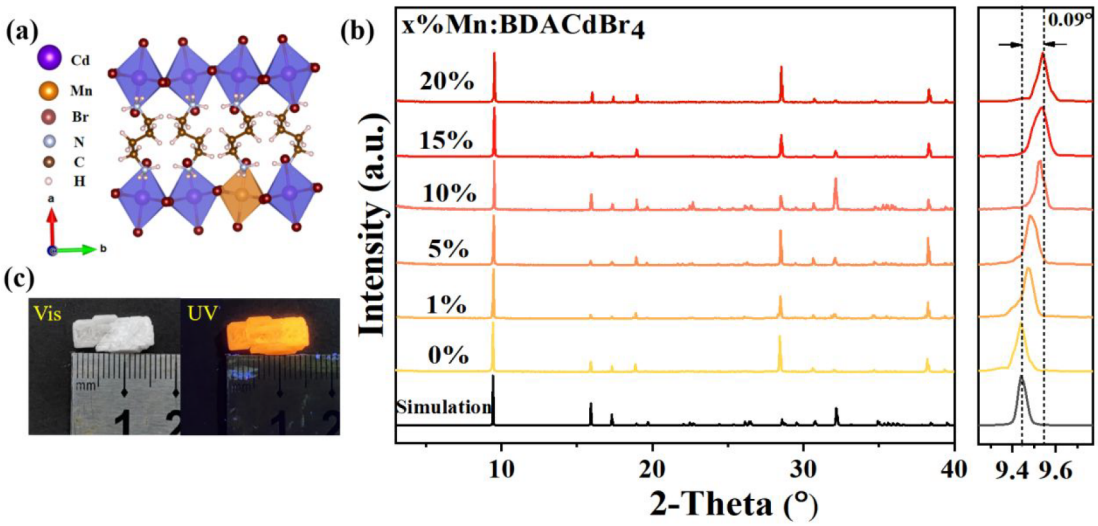

Figure 1. (a) The simulated crystal structure of Mn-doped $BDACdBr_4$, (b) PXRD patterns of Mn-doped $BDACdBr_4$ with different Mn^{2+} feeding concentrations, (c) digital photographs of 15%Mn-doped $BDACdBr_4$ bulk SC under room and UV light (λ_{ex} = 365 nm).

The differences of the photophysical mechanism between Pb^{2+}- and Sb^{3+}-doped $BDACdBr_4$ were revealed through femtosecond transient absorption.[28,29] Likewise, as efficient luminescent dopants, Mn^{2+} ions are widely used to modulate the optical and magnetic properties of doped semiconductors.[30−36] On this basis, Mn^{2+} may be a potentially good candidate for doping $BDACdBr_4$ HLP. However, the effect of Mn^{2+} without the ns^2 electrons on the optical properties of $BDACdBr_4$ still needs further research.

In this work, we successfully prepared highly luminescent Mn-doped $BDACdBr_4$ perovskite SCs with the near-unity PLQY of 96%. The incorporation of Mn^{2+} ions tailors the energy transfer processes and results in strong PL from the Mn $^4T_1(G) \rightarrow {}^6A_1(S)$ transition. A model is proposed to explain competing energy transfer in Mn-doped $BDACdBr_4$. Besides, the LED application with excellent color stability indicates this class of novel materials should be a promising candidate for light-emitting devices. Our results provide new insights into the influence of Mn^{2+} doping on energy transfer and related optical properties of doped HLPs.

2. EXPERIMENTS

2.1. Materials. 1,4-Diaminobutane [$NH_2(CH_3)_4NH_2$, 98%] was purchased from Aladdin; cadmium acetate ($Cd(CH_3COO)_2$, 99%), manganese acetate ($Mn(CH_3COO)_2$, 99%) and hydrobromic acid (HBr, 48 wt %) were purchased from Macklin; ethanol (EtOH, 99%) was purchased from Nanning Blue Sky Experimental Equipment Co., Ltd. All chemicals were used directly without further purification.

2.2. Synthesis of Mn-Doped $BDACdBr_4$ SCs. Mn-doped $BDACdBr_4$ SCs were synthesized by a natural cooling thermal solvent method (Scheme S1). 1.00 mmol of 1,4-butanediamine (BDA), 1.00 mmol of [$Cd(CH_3COO)_2$ + $Mn(CH_3COO)_2$] at a designed feed ratio of x% = Mn/(Cd + Mn) × 100 = 0%, 1%, 3%, 5%, 10%, 15%, and 20%, and 3 mL of HBr were added into a 15 mL glass vial in turn. And then, the mixture solution was heated and stirred at 100 °C and 300 rpm for 0.5 h until it became clear and transparent. Small-size flake SCs precipitated while naturally cooling to room temperature. Finally, the flake SCs were filtered, washed with ethanol, and dried overnight at 60 °C.

2.3. Synthesis of Mn-Doped $BDACdBr_4$ Bulk SCs. High-quality Mn-doped $BDACdBr_4$ bulk SCs were synthesized by a combination of natural cooling thermal solvent and seed crystallization (Scheme S1). A clear precursor solution was obtained by heating and stirring a mixture of BDA/[$Cd(CH_3COO)_2$ + $Mn(CH_3COO)_2$]/HBr = 1.00 mmol:1.00 mmol:3.00 mL at 100 °C and 300 rpm for 0.5 h. And then the hot clear precursor solution was slowly cooled to 50 °C before a small microcrystal was put in the solution as a seed. The solution with a seed was kept at a constant temperature of 50 °C without any disturbance. After 3 d, the seed crystal could grow into a high-quality bulk SC. Finally, the bulk single crystal was filtered, washed with ethanol, and dried overnight at 60 °C.

2.4. Characterizations. The crystal structure was characterized by powder X-ray diffraction (PXRD, Bruker D8 Discover). The morphology of samples was observed by scanning electron microscopy (SEM, Hitachi SU8020). The molar concentrations of Cd^{2+} and Mn^{2+} were detected by inductively coupled plasma atomic emission spectrometry (ICP-AES, ICPE-9000, Shimadzu). Element composition and distribution were collected by energy-dispersive spectrometry (EDS, Oxford X-Max Aztec). The elemental composition and chemical state were identified by X-ray photoelectron spectroscopy (XPS, Thermo Fisher Scientific ESCALAB 250Xi). The photoluminescence (PL) spectra, photoluminescence excitation (PLE) spectra, PL decay profiles, PLQY, temperature-dependent PL spectra, and temperature-dependent PL decay profiles were obtained on an Edinburgh FLS-1000 spectrofluorometer and Horiba Jobin Yvon Fluorolog-3 spectrometer. The absorption spectrum was measured by the Lambda 750 ultraviolet−visible spectrophotometer. The photoelectric properties of the as-fabricated LED device, including the emission spectra, correlated color temperature (CCT), and Commission Internationale de L'Eclairage (CIE) chromaticity coordinate, were obtained on an ATA-1000 (Everfine) optoelectronic analyzer.

3. RESULTS AND DISCUSSION

3.1. Structure of 2D Mn-Doped $BDACdBr_4$ HLPs. 2D Mn-doped $BDACdBr_4$ HLP adopts the crystal space group of monoclinic $P2_1/c$. As shown in Figure 1a, angle-shared inorganic metal octahedral $[CdBr_6]^{4-}$ backbone monolayers stack with organic BDA monolayers, and the Mn^{2+} ions that are introduced partially substitute for Cd^{2+} ions by forming $[MnBr_6]^{4-}$ octahedra in inorganic layers of $BDACdBr_4$. Mn-Doped $BDACdBr_4$ SCs are synthesized by a naturally cooling thermal solvent (see Experimental Materials and Methods). Figure 1b shows the PXRD patterns of 0−20%Mn-doped $BDACdBr_4$. The PXRD pattern of pristine $BDACdBr_4$ sample matches well with the simulated pattern. The absence of additional diffraction peaks confirms the high purity of

https://doi.org/10.1021/acsami.2c13878
ACS Appl. Mater. Interfaces 2022, 14, 45725−45733

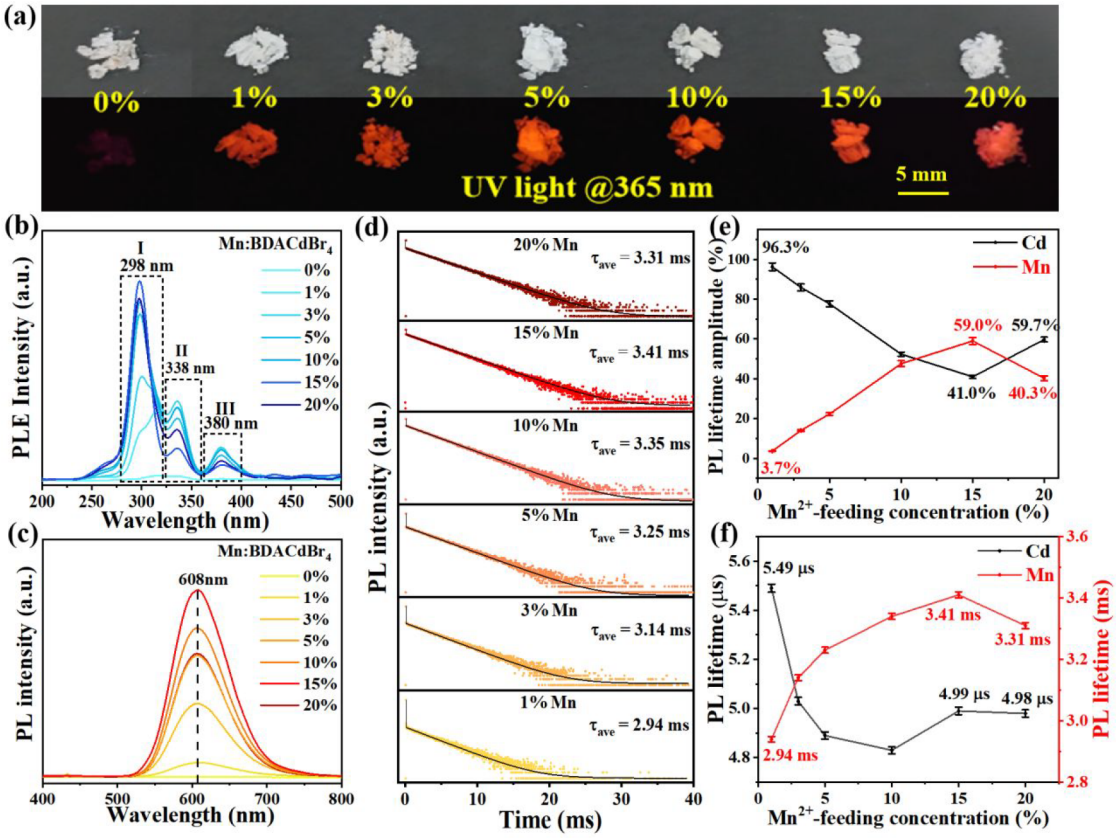

Figure 2. (a) Digital photographs of 0−20%Mn-doped $BDACdBr_4$ SCs under visible and 365 nm UV light, (b) PLE (λ_{em} = 608 nm) and (c) PL (λ_{ex} = 298 nm) spectra of 0−20%Mn-doped $BDACdBr_4$ samples, (d) the PL decay profiles of 1−20%Mn-doped $BDACdBr_4$ samples (λ_{ex} = 298 nm, λ_{em} = 608 nm), (e) the fitting amplitudes of the fast and slow lifetimes in PL decay profiles of 1−20%Mn-doped $BDACdBr_4$ samples, (f) the fitting values of fast and slow lifetimes in PL decay profiles of 1−20%Mn-doped $BDACdBr_4$ samples.

prepared samples. Upon incorporation of Mn^{2+}, the diffraction peak in the range of 9.4−9.6° shifts toward a higher angle, and the maximum offset of 0.09° is reached at 20% Mn^{2+}-feeding concentration. Due to the smaller atomic radius of Mn^{2+} ion (∼0.67 Å) than that of Cd^{2+} ion (∼0.95 Å), the incorporation of Mn^{2+} ions results in lattice contraction and the PXRD diffraction peaks moving toward a higher angle. Furthermore, high-quality large Mn-doped $BDACdBr_4$ bulk SCs were successfully synthesized through a combination of natural cooling thermal solvent and seed crystallization. The SC with a maximum length of ∼15 mm shows a uniform bright orange emission under UV light (Figure 1c), indicating homogeneous distribution of Mn^{2+} in $BDACdBr_4$.

The EDS mapping of 15%Mn-doped $BDACdBr_4$ shows that N, Cd, Mn, and Br elements are evenly distributed in the as-synthesized microcrystal (Figure S1). From total spectrum (Figure S2), the element ratio of N/(Cd+Mn)/Br of 15%Mn-doped $BDACdBr_4$ is very close to the stoichiometric ratio of 2:1:4. Furthermore, the actual doping concentrations of all Mn-doped samples were detected by ICP-AES. As shown in Table S1, the actual doping concentration is lower than the feeding concentration, especially for Mn^{2+} feeding concentration greater than 10%. Figure S3 shows XPS results of pristine and 15%Mn-doped $BDACdBr_4$. In the survey spectra, the shared peaks of N 1s, Cd 3d, and Br 3d in pristine and 15% Mn-doped samples can be clearly observed, while Mn 2p characteristic peaks can only be observed in the 15%Mn-doped sample. Figure S4a−c shows the high-resolution XPS spectra and peak fitting of N 1s, Cd 3s, and Br 3d in the pristine and 15%Mn-doped samples. Mn^{2+} doping slightly increases the electron binding energy around N, Cd, and Br, indicating stronger binding and more compact electron distribution. From Figure S4d, the new peaks at 652.1 and 641.9 eV are attributed to $2P_{1/2}$ and $2P_{3/2}$ of Mn^{2+} dopants.

3.2. Optical Properties of 2D Mn-Doped $BDACdBr_4$ HLPs. Figure 2a shows digital photographs of 0−20%Mn-doped $BDACdBr_4$ SCs under visible and 365 nm UV light. The pristine $BDACdBr_4$ SC exhibits a faint emission, while the introduction of Mn^{2+} ions results in a strong orange emission. From the absorption spectra (Figure S5), the pristine $BDACdBr_4$ exhibits a weak flat absorption tail in the range of 300−650 nm. Three bands that peaked at 316, 338, and 380 nm and a weak shoulder at 298 nm are observed in the PLE spectra of the pristine $BDACdBr_4$ by monitoring the 625 nm emission (Figure S6a). According to previous reports,[28,29] the three bands at 316, 338, and 380 nm are assigned to the spin-forbidden and parity-allowed $^1A_{1g} \rightarrow {}^3E_g$ triplet-to-singlet transition absorptions of Cd^{2+}, while the weak shoulder at 298 nm derives from the absorption transition of the $BDACdBr_4$ perovskite host. A weak broad emission band peak at 625 nm is observed under 338 nm excitation (Figure S6b), which has an average PL lifetime of ∼4.67 μs (Figure S7), consistent with triplet $^3E_g \rightarrow {}^1A_{1g}$ transition emission of Cd^{2+}.[37−39]

As for the 15%Mn-doped $BDACdBr_4$ sample, a series of new absorption bands are observed in the 300−650 nm region, attributed to transitions from the ground state $^6A_1(S)$ to excited states $^4E(D)$, [^4E (G),$^4A_1(G)$], $^4A_1(G)$, $^4T_2(G)$, and $^4T_1(G)$ of Mn^{2+} ions (Figure S5).[32,37,38] From the PLE spectra

https://doi.org/10.1021/acsami.2c13878
ACS Appl. Mater. Interfaces 2022, 14, 45725−45733

(Figure 2b), a strong excitation band peak at 298 nm appears after Mn^{2+} incorporation and is labeled as band I. With increasing Mn^{2+} feeding concentration, the intensity of band I increases substantially and reaches the highest value at 15% Mn^{2+} feeding concentration (Figure S8). Based on similar works,[29] the intensified band I induced by Mn^{2+} incorporation is attributed to the fact that the energy absorbed by the host is transferred to Mn^{2+} d-state for relaxation. In addition, the two other excitation bands that peaked at 338 and 380 nm labeled as bands II and III are assigned to the $^1A_{1g} \rightarrow {}^3E_g$ triplet transition absorption of Cd^{2+}.[28,29,40] The incorporation of Mn^{2+} ions also enhances the photoexcitation intensity of these two bands, possibly related to the overlapping self-absorption of Mn^{2+} ions.

With respect to the weak emission of a pristine sample, all Mn^{2+}-doped samples show an intense orange emission at 608 nm under 298 nm (band I) excitation (Figure 2c). This orange emission has a narrower full width at half maxima (fwhm) value (~0.28 eV) compared to the emission of a pristine sample (~0.59 eV) (Figure S9), which is attributed to the introduction of d-d transition emission from Mn^{2+} dopants.[41−43] The pristine sample exhibits a low PLQY (<1%), while the incorporation of Mn^{2+} ions greatly improves the emission efficiency, and a near-unity value (~96%) is achieved for the 15%Mn-doped sample. However, the sample with excessive Mn-feeding concentration (20%Mn) shows a low PLQY (~60%) due to the effect of concentration quenching (Figure S10).

Figure 2d shows the PL decay profiles monitored at 608 nm emission for all Mn-doped $BDACdBr_4$ samples, and the fitting parameters are summarized in Table S2. All the PL decay profiles are composed of a fast microsecond decay component and slow millisecond decay one. The slow millisecond component originates from the spin-forbidden $^4T_1(G) \rightarrow {}^6A_1(S)$ transition of Mn^{2+},[44] while the fast microsecond component should be attributed to the $^3E_g \rightarrow {}^1A_{1g}$ transition of Cd^{2+} (Figure S7).[29,40] Interestingly, the fast microsecond component is still retained in all PL decay profiles of Mn-doped samples, indicating the introduction of Mn^{2+} ions does not completely quench the $^3E_g \rightarrow {}^1A_{1g}$ triplet emission of Cd^{2+}. The fitting amplitudes and lifetimes of decay profiles of all Mn-doped samples are shown in Figure 2e,f, respectively. As the Mn^{2+} feeding concentration increases from 1% to 15%, an increase in the amplitude of millisecond PL lifetime from Mn^{2+} is accompanied by a decrease in the amplitude of microsecond PL lifetime from Cd^{2+}, suggesting the emission from Mn^{2+} gradually becomes dominant. As the Mn^{2+} feeding concentration reaches 15%, the PL lifetime and amplitude of Mn^{2+} emission achieve the highest values of 3.41 ms and 59.0%, respectively. The average PL lifetime of 15%Mn-doped $BDACdBr_4$ is also 3.41 ms due to the large amplitude of millisecond PL lifetime, indicating the emission from Mn^{2+} has a great contribution to the overall luminescence under excitation of band I excitation. However, for higher Mn^{2+} concentration (20%Mn), the lifetime and amplitude of Mn^{2+} emission are reduced to 3.32 ms and 40.3%, respectively, which is probably related to the self-absorption quenching resulting from the formation of Mn^{2+}-Mn^{2+} pairs.[31,45]

3.3. Excitation Wavelength-Dependent Spectroscopic Characterization and Mechanism of Energy Transfer. To investigate the underlying emission mechanism of Mn-doped $BDACdBr_4$, emission wavelength-dependent PLE spectra and excitation wavelength-dependent PL spectra were measured. As shown in emission wavelength-dependent PLE spectra (Figure 3a), the bands II and III fall more slowly

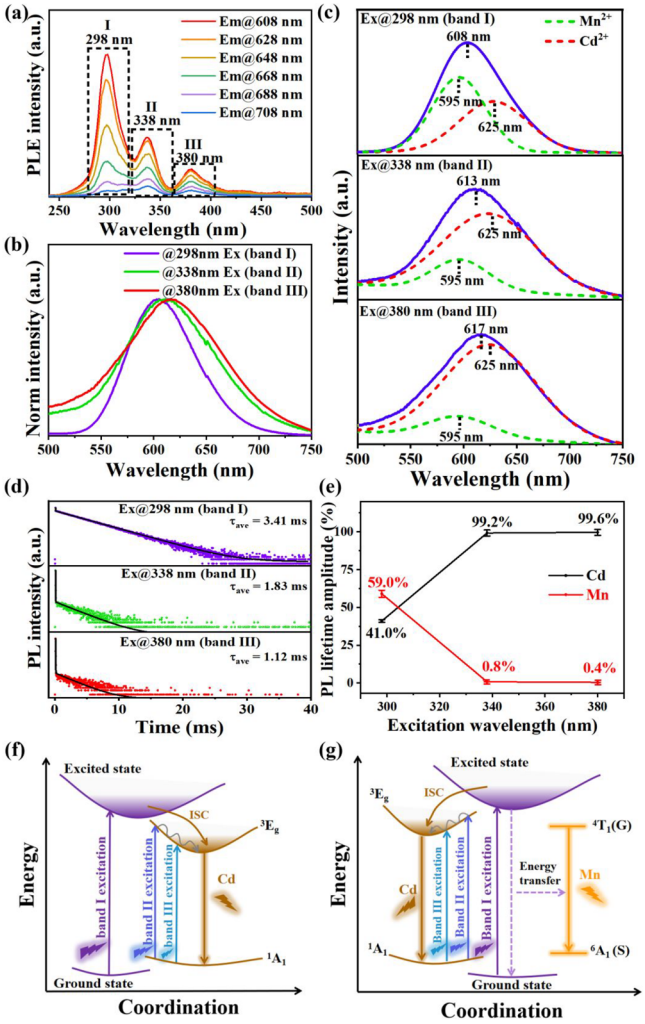

Figure 3. (a) PLE spectra of 15%Mn-doped $BDACdBr_4$ with different monitored emission wavelengths (λ_{em} = 608−708 nm). (b) Normalized PL spectra with different excitation wavelengths (λ_{ex} = 298−380 nm). (c) Deconvolution of PL bands. (d) PL decay profiles and (e) the fitting amplitudes of the fast and slow PL lifetimes in PL decay profiles of 15%Mn-doped $BDACdBr_4$ upon different excitation wavelengths (λ_{ex} = 298−380 nm, λ_{em} = 608 nm), and the schematic photophysical mechanism of (f) pristine and (g) Mn-doped $BDACdBr_4$.

than band I as the monitored emission wavelength is changed from 608 to 708 nm. The synchronous changes of bands II and III indicate the same physical emission origin, while band I derives from another excited state of the host. Consistent with normalized excitation wavelength-dependent PL spectra (Figure 3b), the PL band becomes wider and red-shifted upon excitation wavelength changing from band I to III, further indicating the existence of other emission centers besides Mn^{2+} in Mn-doped $BDACdBr_4$.

To determine the contribution from the different emission centers in PL of Mn-doped $BDACdBr_4$, the emission spectra were deconvoluted as shown in Figure 3c. The PL band consists of two broad emissions that peaked at 595 and 625 nm, respectively. Moreover, the contribution from the emission peak at 625 nm improves sharply upon excitation

https://doi.org/10.1021/acsami.2c13878
ACS Appl. Mater. Interfaces 2022, 14, 45725−45733

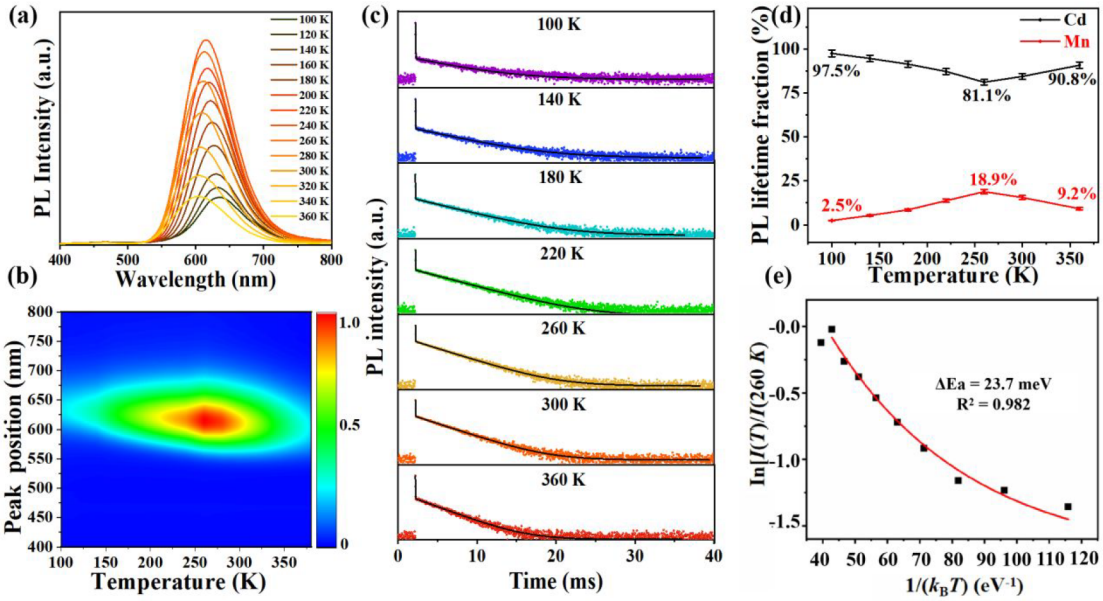

Figure 4. (a) The temperature-dependent PL spectra, (b) pseudocolor map, (c) temperature-dependent PL decay profiles, (d) fitting amplitudes of the fast and slow PL lifetimes of Mn-doped $BDACdBr_4$ (T = 100−360 K, λ_{ex} = 298 nm), and (e) Boltzmann analysis of the integrated PL intensity above a function of thermal activation temperature (k_BT) yields an activation energy $\Delta E_a \approx 23.7$ meV.

changing from band I to III. The emission peak at 625 nm should derive from the Cd^{2+} $^3E_g \rightarrow {}^1A_{1g}$ transition,[29,40] while another emission peak at 595 nm probably comes from the Mn^{2+} $^4T_1(G) \rightarrow {}^6A_1(S)$ transition. The PL decay spectra and fitting parameters confirm the attributions of two emission bands (Figure 3d, Table S3), in which both Mn^{2+} and Cd^{2+} PL lifetimes coexist throughout the whole relaxation process. The evolution of PL is attributed to the variation of contributions of Mn^{2+} and Cd^{2+} emissions (Figure 3c). Upon excitation at band I, the millisecond PL lifetime has a larger amplitude (~59.0%) (Figure 3e), indicating the recombination of excitons via Mn^{2+} d-d transition dominants. The higher proportion of Mn^{2+} emission component results in PL with a narrow fwhm and a blue-shifted peak position (Figure 3b). However, upon longer excitation wavelengths at bands II and III, the microsecond PL lifetime has a near-unity amplitude (~99.2−99.6%) (Figure 3e), indicating that the PL of Mn-doped $BDACdBr_4$ is mainly contributed from the Cd^{2+} $^3E_g \rightarrow {}^1A_{1g}$ transition emission component, whose PL band becomes wider and red-shifted (Figure 3b).

Based on the above discussion, a schematic illustration of the photophysical mechanisms behind the optical properties of pristine $BDACdBr_4$ is given in Figure 3f. Under excitation at band I, electrons are excited from the valence band (VB) to the conduction band (CB) of the $BDACdBr_4$ host. However, upon excitation at bands II and III, electronic transition into the ^3E_g state of Cd^{2+} occurs. In the meantime, the electrons in the excited state of the host can intersystem-cross (ISC) to the ^3E_g state of Cd^{2+}. Therefore, all excited states have the same relaxation process ($^3E_g \rightarrow {}^1A_{1g}$) back to the ground state. The photophysical mechanism of Mn-doped $BDACdBr_4$ is shown schematically in Figure 3g. Upon excitation at band I of the host, energy transfer from the excited state of the host to Mn dopants results in emission from the $^4T_1(G) \rightarrow {}^6A_1(S)$ transition with a near-unity PLQY. However, when the excitation wavelength is changed to bands II and III, the ^3E_g state of Cd^{2+} is excited. The photoexcited energy mainly relaxes via the Cd $^3E_g \rightarrow {}^1A_{1g}$ transition, similar to the pristine sample PL.

3.4. PL Thermal Activation in Mn-doped $BDACdBr_4$ HLPs. Figure 4a,b shows the temperature-dependent PL spectra and corresponding pseudocolor map in the range of 100−360 K. Unlike the behaviors of the temperature-dependent PL of metal ions with ns^2 electron configuration (such as Sb^{3+}),[29,46] the main PL peak blue-shifts significantly, and the PL intensity exhibits a volcano-like change with increasing temperature. The detailed changes in the PL peak position and intensity are clearly shown in Figure S11. Throughout the heating process, the thermal expansion of the lattice can reduce the crystal field intensity and result in an increase in the $^4T_1(G) \rightarrow {}^6A_1(S)$ transition energy of Mn^{2+} ions; thus, the emission peak blue-shifts.[47]

The PL intensity increases in the range of 100−260 K and decreases in the range of 260−360 K with increasing temperature. To clarify the change of this anomalous PL intensity, temperature-dependent PL decay curves are collected in Figure 4c, and the detailed fitting parameters are shown in Table S4. The low-temperature environment is more conducive to the radiative recombination due to the weakening of phonon scattering and fewer defects. Thus, the emission from Cd^{2+} and Mn^{2+} dopants have longer PL lifetimes of 16.13 μs and 5.47 ms at 100 K, respectively (Figure S12). The emission from Mn^{2+} is the critical component of the PL of Mn-doped $BDACdBr_4$ under excitation of band I (Figure 3c). However, the amplitude of the Mn^{2+} PL lifetime is only 2.5% at 100 K (Figure 4d), which is responsible for the low PL intensity at low temperature. Based on previous studies,[37,48,49] the temperature dependence of the Mn^{2+} PL arises from vibronic activation of the radiative d-d transition. With increasing temperature from 100 to 260 K, the sensitization of the Mn^{2+} d-d transition is gradually thermally activated by lattice vibration, so that an increase in emission intensity can be observed. The thermal activation energy (E_a) required for transferring excitons from host to Mn^{2+} dopants can be estimated using a Boltzmann analysis of the integrated PL

https://doi.org/10.1021/acsami.2c13878
ACS Appl. Mater. Interfaces 2022, 14, 45725−45733

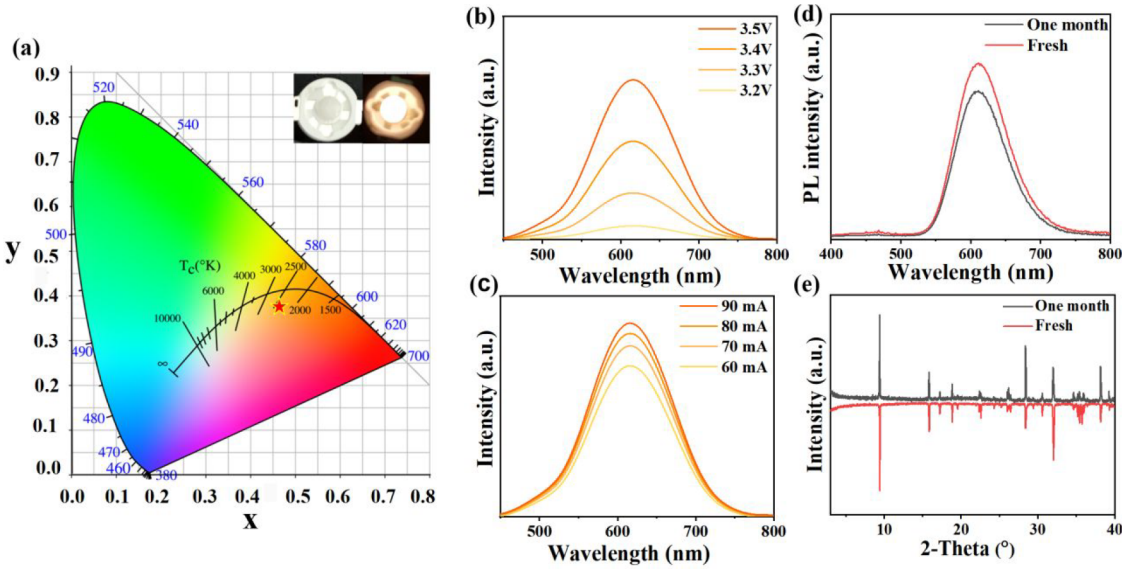

Figure 5. (a) CIE chromaticity diagram of the LED lamp. Inset images are the photos of LED lamp off (left) and on (right), (b) PL spectra with different driving voltages, (c) PL spectra with different driving currents, and (d) PL spectra and (e) XRD patterns of fresh and air-exposed for one month samples.

intensity as a function of temperature ($1/k_BT$) through the following equation[50−52]

$$I_{Mn}(T) = I_0 \cdot e^{-\Delta E_a/k_BT} \quad (1)$$

where $I_{Mn}(T)$ is the integrated PL intensity at different temperature (100−280 K) and k_B is the Boltzmann constant. The ΔE_a of Mn-doped $BDACdBr_4$ is calculated to be ∼23.7 meV at 260 K (Figure 4e), which is comparable with the thermal energy of ∼22.4 meV at 260 K (k_BT). Such a small potential barrier enables the efficient transfer of excitons to Mn^{2+} dopants and leads to maximum PL intensity. It is well-known that high temperature usually results in PL quenching due to thermal quenching. Therefore, further increasing the temperature from 260 to 360 K will reduce the PL intensity.

3.5. Electronic Band Structure of Mn-Doped $BDACdBr_4$ HLPs. Based on the crystal structure of pristine $BDACdBr_4$ (Figure S13a), we modeled the structure of Mn-doped $BDACdBr_4$ by replacing Cd^{2+} with Mn^{2+} equivalently (Figure S13b). Comparing the bond lengths between triad angle-shared $[CdBr_6]^{4-}$-$[CdBr_6]^{4-}$-$[CdBr_6]^{4-}$ and $[CdBr_6]^{4-}$-$[MnBr_6]^{4-}$-$[CdBr_6]^{4-}$ octahedra (Figure S13c,d), Mn^{2+} incorporation results in a more compact inorganic metal layer, which is mainly manifested in a shorter Mn−Br bond that brings the $[MnBr_6]^{4-}$ octahedra closer to the $[MnBr_6]^{4-}$ octahedra.

First-principle calculations based on density functional theory (DFT) are carried out to investigate the electronic band structures of pristine and Mn-doped $BDACdBr_4$. The band structure of pristine $BDACdBr_4$ is consistent with that of a recent report and exhibits an indirect band gap of about 2.83 eV (Figure S14a).[28,29] Due to the indirect band gap nature of the pristine $BDACdBr_4$, the PL process is dipole-forbidden. From the density of states (DOS) of pristine $BDACdBr_4$ (Figure S14b), the conduction band minimum (CBM) mainly consists of the Cd-s and Br-p orbitals, while Br-p orbital is the main component of the valence band maximum (VBM). The incorporation of Mn^{2+} introduces new localized Mn-d and Br-p orbitals in the band gap (Figure S14c), which facilitates energy transfer to the Mn^{2+} orbital during the relaxation process from CBM to VBM. Besides, the VB of Mn-doped $BDACdBr_4$ is relatively flat, leading to strong localization of the holes. The DOS of Mn-doped $BDACdBr_4$ shows that the Mn-3d orbital contributes little to the VB, but it hybridizes with Br-p and Cd-s orbitals of the host elements in the CB (Figure S14d), which enables the energy absorbed by the host to easily transfer to Mn, thus allowing for radiative d-d transition.

3.6. LED Lamp and Stability of Mn-Doped $BDACdBr_4$ HLPs. The LED based on 15%Mn-doped $BDACdBr_4$ powder shows excellent color stability and emits stable bright orange light under different driving voltages and currents. The color coordinates of emission based on CIE 1931 is (0.4658,0.3784) with a correlated color temperature (CCT) of 2366 K (Figure 5a−c). These results show that Mn-doped $BDACdBr_4$ HLPs is promising for solid-state lighting and backlight displays.

The fresh samples were ground into powder and completely exposed to air with a humidity of about 50−70% for one month. The PL intensity did not attenuate significantly and remained above 80% of the initial value (Figure 5d). To determine whether the sample decomposed, we compared the PXRD pattern of the fresh sample with the sample exposed to air for a month (Figure 5e). Their PXRD patterns are almost the same with no impurity diffraction peaks observed, indicating good stability of the Mn-doped $BDACdBr_4$ HLPs in air.

4. CONCLUSION

In summary, we have successfully prepared Mn-doped $BDACdBr_4$ SCs with different doping concentrations (1−20%). The incorporation of Mn^{2+} ions modulates the electronic band structure of $BDACdBr_4$ and tailors the relaxation energy of excited states, resulting in an orange emission at 608 nm with near-unity PLQY of 96%. The underlying energy transfer mechanisms in pristine and Mn-doped $BDACdBr_4$ are determined through excitation wavelength-dependent spectral studies. Competing energy transfer processes between $^3E_g \rightarrow {}^1A_{1g}$ of Cd^{2+} and $^4T_1(G) \rightarrow {}^6A_1(S)$ of Mn^{2+} affect the overall emission process of Mn-doped $BDACdBr_4$. The solid-state lighting LED prepared using 15%

https://doi.org/10.1021/acsami.2c13878
ACS Appl. Mater. Interfaces 2022, 14, 45725−45733

Mn-doped $BDACdBr_4$ powder shows good luminous performance and color stability, indicating this class of novel materials should be a promising candidate for light-emitting devices. Our results provide new insight for the photophysics of 2D HLPs, especially the influence of Mn^{2+} dopant on energy transfer in luminescent hybrid materials with potential application in optoelectronics.

■ ASSOCIATED CONTENT

Supporting Information

The Supporting Information is available free of charge at https://pubs.acs.org/doi/10.1021/acsami.2c13878.

Additional experimental details and data, including the computational details, the preparation of LED lamp, schematic illustration of the synthesis, SEM image, EDS mapping, ICP-AES results, XPS spectra, absorption spectra, the change of excitation bands intensity, PL spectra, PLQY, PL lifetime tables, peak position and intensity of temperature-dependent PL, temperature-dependent fitting PL lifetime, the crystal structure, the electronic band structures and DOS (PDF)

■ AUTHOR INFORMATION

Corresponding Authors

Ruosheng Zeng − *School of Physical Science and Technology, MOE Key Laboratory of New Processing Technology for Non-ferrous Metals and Materials, Guangxi Key Laboratory of Processing for Non-ferrous Metals and Featured Materials, Guangxi University, Nanning 530004, China;* orcid.org/0000-0002-8536-326X; Email: zengrsh@guet.edu.cn

Jin Zhong Zhang − *Department of Chemistry and Biochemistry, University of California, Santa Cruz 95064 California, United States;* orcid.org/0000-0003-3437-912X; Email: Zhang@ucsc.edu

Authors

Canxu Chen − *School of Physical Science and Technology, MOE Key Laboratory of New Processing Technology for Non-ferrous Metals and Materials, Guangxi Key Laboratory of Processing for Non-ferrous Metals and Featured Materials, Guangxi University, Nanning 530004, China*

Shuai Zhang − *School of Physical Science and Technology, MOE Key Laboratory of New Processing Technology for Non-ferrous Metals and Materials, Guangxi Key Laboratory of Processing for Non-ferrous Metals and Featured Materials, Guangxi University, Nanning 530004, China*

Binbin Luo − *Department of Chemistry and Key Laboratory for Preparation and Application of Ordered Structural Materials of Guangdong Province, Shantou University, Shantou 515063 Guangdong, China;* orcid.org/0000-0001-9652-7998

Yuanjie Chen − *School of Physical Science and Technology, MOE Key Laboratory of New Processing Technology for Non-ferrous Metals and Materials, Guangxi Key Laboratory of Processing for Non-ferrous Metals and Featured Materials, Guangxi University, Nanning 530004, China*

Sheng Cao − *School of Physical Science and Technology, MOE Key Laboratory of New Processing Technology for Non-ferrous Metals and Materials, Guangxi Key Laboratory of Processing for Non-ferrous Metals and Featured Materials, Guangxi University, Nanning 530004, China;* orcid.org/0000-0002-6203-9088

Jialong Zhao − *School of Physical Science and Technology, MOE Key Laboratory of New Processing Technology for Non-ferrous Metals and Materials, Guangxi Key Laboratory of Processing for Non-ferrous Metals and Featured Materials, Guangxi University, Nanning 530004, China*

Bingsuo Zou − *School of Physical Science and Technology, MOE Key Laboratory of New Processing Technology for Non-ferrous Metals and Materials, Guangxi Key Laboratory of Processing for Non-ferrous Metals and Featured Materials, Guangxi University, Nanning 530004, China;* orcid.org/0000-0003-4561-4711

Complete contact information is available at: https://pubs.acs.org/10.1021/acsami.2c13878

Notes

The authors declare no competing financial interest.

■ ACKNOWLEDGMENTS

This work was supported by the National Natural Science Foundation of China (22175043, 52162021), the Natural Science Foundation of Guangxi Province (2017GXNSFGA198005), and the special fund for "Guangxi Bagui Scholars". J.Z.Z. is grateful to the United States National Science Foundation for financial support (CHE-2203633). B.L. is thankful for the financial support from the Open Foundation of Guangxi Key Laboratory of Processing for Nonferrous Metals and Featured Materials (Grant No. 2022GXYSOF14). The calculation was supported by the high-performance computing platform of Guangxi University.

■ REFERENCES

(1) Mao, L.; Stoumpos, C. C.; Kanatzidis, M. G. Two-Dimensional Hybrid Halide Perovskites: Principles and Promises. *J. Am. Chem. Soc.* **2019**, *141*, 1171−1190.

(2) Gu, Z.; Wang, Y.; Wang, S.; Zhang, T.; Zhao, R.; Hu, X.; Huang, Z.; Su, M.; Xu, Q.; Li, L.; Zhang, Y.; Song, Y. Controllable Printing of Large-scale Compact Perovskite Films for Flexible Photodetectors. *Nano Res.* **2022**, *15*, 1547−1553.

(3) Chen, H.; Wang, H.; Wu, J.; Wang, F.; Zhang, T.; Wang, Y.; Liu, D.; Li, S.; Penty, R. V.; White, I. H. Flexible Optoelectronic Devices Based on Metal Halide Perovskites. *Nano Res.* **2020**, *13*, 1997−2018.

(4) Zhang, L.; Yuan, M. Lanthanide Doped Lead-Free Double Perovskites as the Promising Next Generation Ultra-Broadband Light Sources. *Light-Sci. Appl.* **2022**, *11*, 99.

(5) Bae, Y.; Ryu, J.; Yoon, S.; Kang, D. Recent Progress in Quasi-Two-Dimensional and Quantum Dot Perovskite Light-Emitting Diodes Harnessing the Diverse Effects of Ligands: a Review. *Nano Res.* **2022**, *15*, 6449−6465.

(6) Correa-Baena, J.-P.; Abate, A.; Saliba, M.; Tress, W.; Jesper Jacobsson, T.; Gratzel, M.; Hagfeldt, A. The Rapid Evolution of Highly Efficient Perovskite Solar Cells. *Energy Environ. Sci.* **2017**, *10*, 710−727.

(7) Kim, J. Y.; Lee, J.; Jung, H. S.; Shin, H.; Park, N. High-Efficiency Perovskite Solar Cells. *Chem. Rev.* **2020**, *120*, 7867−7918.

(8) Gong, Y.; Yu, R.; Gao, H.; Ma, Z.; Dong, Y.; Su, Y.; Chen, T.; Hsu, C.; Tan, Z. Improving Charge Transport and Reducing Non-Radiative Energy Loss via a Nonacyclic Carbazole-Based Third Component for over 18% Efficiency Polymer Solar Cells. *J. Mater. Chem. A* **2022**, *10*, 7090−7098.

(9) Ren, M.; Cao, S.; Zhao, J.; Zou, B.; Zeng, R. Advances and Challenges in Two-Dimensional Organic-Inorganic Hybrid Perovskites Toward High-Performance Light-Emitting Diodes. *Nano-Micro Lett.* **2021**, *13*, 40−75.

(10) Zhang, F.; Zhang, X.; Wang, C.; Sun, M.; Luo, X.; Yang, Y.; Chang, S.; Zhang, D.; Duan, L. Chlorine Distribution Management

for Spectrally Stable and Efficient Perovskite Blue Light-Emitting Diodes. *Nano Energy* **2021**, *79*, 105486.
(11) Li, M.; Zhao, Y.; Qin, X.; Ma, Q.; Lu, J.; Lin, K.; Xu, P.; Li, Y.; Feng, W.; Zhang, W.; Wei, Z. Conductive Phosphine Oxide Passivator Enables Efficient Perovskite Light-Emitting Diodes. *Nano Lett.* **2022**, *22*, 2490−2496.
(12) Luo, J.; Yang, L.; Tan, Z.; Xie, W.; Sun, Q.; Li, J.; Du, P.; Xiao, Q.; Wang, L.; Zhao, X.; Niu, G.; Gao, L.; Jin, S.; Tang, J. Efficient Blue Light Emitting Diodes Based on Europium Halide Perovskites. *Adv. Mater.* **2021**, *33*, 2101903.
(13) Tian, W.; Zhou, H.; Li, L. Hybrid Organic-Inorganic Perovskite Photodetectors. *Small* **2017**, *13*, 1702107.
(14) Zhang, Y.; Ma, Y.; Wang, Y.; Zhang, X.; Zuo, C.; Shen, L.; Ding, L. Lead-Free Perovskite Photodetectors: Progress, Challenges, and Opportunities. *Adv. Mater.* **2021**, *33*, 2006691.
(15) Yu, D.; Cao, F.; Gu, Y.; Han, Z.; Liu, J.; Huang, B.; Xu, X.; Zeng, H. Broadband and Sensitive Two-Dimensional Halide Perovskite Photodetector for Full-Spectrum Underwater Optical Communication. *Nano Res.* **2021**, *14*, 1210−1217.
(16) Ma, L.; Dai, J.; Zeng, X. C. Two-Dimensional Single-Layer Organic-Inorganic Hybrid Perovskite Semiconductors. *Adv. Energy Mater.* **2017**, *7*, 1601731.
(17) Liu, F.; Zhang, T.; Mondal, D.; Teng, S.; Zhang, Y.; Huang, K.; Wang, D.; Yang, W.; Mahadevan, P.; Zhao, Y.; Xie, R.; Pradhan, N. Light-Emitting Metal-Organic Halide 1D and 2D Structures: Near-Unity Quantum Efficiency, Low-Loss Optical Waveguide and Highly Polarized Emission. *Angew. Chem.-Int. Ed.* **2021**, *60*, 13548−13553.
(18) Kieslich, G.; Sun, S.; Cheetham, A. K. Solid-State Principles Applied to Organic-Inorganic Perovskites: New Tricks for an Old Dog. *Chem. Sci.* **2014**, *5*, 4712−4715.
(19) Shi, C.; Yu, C.-H.; Zhang, W. Predicting and Screening Dielectric Transitions in a Series of Hybrid Organic-Inorganic Double Perovskites via an Extended Tolerance Factor Approach. *Angew. Chem.-Int. Ed.* **2016**, *55*, 5798−5802.
(20) Fu, P.; Sun, Y.; Xia, Z.; Xiao, Z. Photoluminescence Behavior of Zero-Dimensional Manganese Halide Tetrahedra Embedded in Conjugated Organic Matrices. *J. Phys. Chem. Lett.* **2021**, *12*, 7394−7399.
(21) Xu, Y.; Cao, M.; Huang, S. Recent Advances and Perspective on the Synthesis and Photocatalytic Application of Metal Halide Perovskite Nanocrystals. *Nano Res.* **2021**, *14*, 3773−3794.
(22) Xu, K.; Vickers, E. T.; Luo, B.; Wang, Q.; Allen, A. C.; Wang, H.; Cherrette, V.; Li, X.; Zhang, J. Z. Room Temperature Synthesis of Cesium Lead Bromide Perovskite Magic Sized Clusters with Controlled Ratio of Carboxylic Acid and Benzylamine Capping Ligands. *Sol. Energy Mater. Sol. C* **2020**, *208*, 110341.
(23) Geim, A. K.; Grigorieva, I. V. Van der Waals Heterostructures. *Nature* **2013**, *499*, 419−425.
(24) Mitzi, D. B. Synthesis, Crystal Structure, and Optical and Thermal Properties of $(C_4H_9NH_3)_2MI_4$ (M = Ge, Sn, Pb). *Chem. Mater.* **1996**, *8*, 791−800.
(25) Dou, L.; Wong, A. B.; Yu, Y.; Lai, M.; Kornienko, N.; Eaton, S. W.; Fu, A.; Bischak, C. G.; Ma, J.; Ding, T.; Ginsberg, N. S.; Wang, L.; Alivisatos, A. P.; Yang, P. Atomically Thin Two-Dimensional Organic-Inorganic Hybrid Perovskites. *Science* **2015**, *349*, 1518−1521.
(26) Tan, Z.; Wu, Y.; Hong, H.; Yin, J.; Zhang, J.; Lin, L.; Wang, M.; Sun, X.; Sun, L.; Huang, Y.; Liu, K.; Liu, Z.; Peng, H. Two-Dimensional $(C_4H_9NH_3)_2PbBr_4$ Perovskite Crystals for High-Performance Photodetector. *J. Am. Chem. Soc.* **2016**, *138*, 16612−16615.
(27) Wang, Y.; Ji, C.; Liu, X.; Han, S.; Zhang, J.; Sun, Z.; Khan, A.; Luo, J. (1,4-Butyldiammonium)$CdBr_4$: a Layered Organic-Inorganic Hybrid Perovskite with a Visible-Blind Ultraviolet Photoelectric Response. *Inorg. Chem. Front.* **2018**, *5*, 2450−2455.
(28) Liang, D.; Lian, X.; Li, X.; Luo, B. Pb Alloying Enables Efficient Broadband Emission of Two Dimensional $[NH_3(CH_2)_4NH_3]CdBr_4$. *J. Solid State Chem.* **2021**, *293*, 121772.
(29) Wu, J.; Li, X.; Lian, X.; Su, B.; Pang, J.; Li, M.; Xia, Z.; Zhang, J. Z.; Luo, B.; Huang, X. Ultrafast Study of Exciton Transfer in Sb(III)-Doped Two-Dimensional $[NH_3(CH_2)_4NH_3]CdBr_4$ Perovskite. *ACS Nano* **2021**, *15*, 15354−15361.
(30) Yan, J.; Zhang, S.; Wei, Q.; Cao, S.; Zhao, J.; Zou, B.; Zeng, R. Stoichiometry-Controlled Phase Engineering of Cesium Bismuth Halides and Reversible Structure Switch. *Adv. Opt. Mater.* **2022**, *10*, 2101406.
(31) Peng, C.; Wei, Q.; Chen, L.; Zeng, R.; Zhang, Q.; Hu, Q.; Zou, B. Efficient Energy Transfer in $Cs_4Mn_xCd_{1-x}Sb_2Cl_{12}$ Layered Perovskites and Anomalously Responsive Photodetectors. *J. Mater. Chem. C* **2021**, *9*, 15522−15529.
(32) Su, B.; Molokeev, M. S.; Xia, Z. Unveiling Mn^{2+} Dopant States in Two-Dimensional Halide Perovskite toward Highly Efficient Photoluminescence. *J. Phys. Chem. Lett.* **2020**, *11*, 2510−2517.
(33) Vargas, B.; Reyes-Castillo, D. T.; Coutino-Gonzalez, E.; Sanchez-Ake, C.; Ramos, C.; Falcony, C.; Solis-Ibarra, D. Enhanced Luminescence and Mechanistic Studies on Layered Double-Perovskite Phosphors: $Cs_4Cd_{1-x}Mn_xBi_2Cl_{12}$. *Chem. Mater.* **2020**, *32*, 9307−9315.
(34) Ren, J.; Zhou, X.; Wang, Y. Water Triggered Interfacial Synthesis of Highly Luminescent $CsPbX_3$:Mn^{2+} Quantum Dots from Nonluminescent Quantum Dots. *Nano Res.* **2020**, *13*, 3387−3395.
(35) Wang, P.; Dong, B.; Cui, Z.; Gao, R.; Su, G.; Wang, W.; Cao, L. Synthesis and Characterization of Mn-doped $CsPb(Cl/Br)_3$ Perovskite Nanocrystals with Controllable Dual-Color Emission. *RSC Adv.* **2018**, *8*, 1940−1947.
(36) Xu, K.; Vickers, E. T.; Luo, B.; Allen, A. L. C.; Chen, E.; Roseman, G.; Wang, Q.; Kliger, D. S.; Millhauser, G. L.; Yang, W.; Li, X.; Zhang, J. First Synthesis of Mn-Doped Cesium Lead Bromide Perovskite Magic Sized Clusters at Room Temperature. *J. Phys. Chem. Lett.* **2020**, *11*, 1162−1169.
(37) Yu, Z.; Peng, H.; Wei, Q.; Huang, T.; Yao, S.; Tian, Y.; Peng, C.; Zou, B. The Magnetic Polaron Modulated Luminescence Bands of Organic-Inorganic Hybrid Ferroelectric Anti-Perovskite $(C_3H_9N)_3Cd_2Cl_7$ Doped with Mn^{2+}. *Mater. Today Chem.* **2022**, *24*, 100781.
(38) Jia, W.; Wei, Q.; Ge, S.; Peng, C.; Huang, T.; Yao, S.; Tian, Y.; Chang, T.; Zeng, R.; Zou, B. Polaronic Magnetic Excitons and Photoluminescence in Mn^{2+}-Doped $CsCdBr_3$ Metal Halides. *J. Phys. Chem. C* **2021**, *125*, 18031−18039.
(39) Jin, J.; Peng, Y.; Xu, Y.; Han, K.; Zhang, A.; Yang, X.; Xia, Z. Bright Green Emission from Self-Trapped Excitons Triggered by Sb^{3+} Doping in Rb_4CdCl_6. *Chem. Mater.* **2022**, *34*, 5717−5725.
(40) Cai, T.; Yang, H.; Hills-Kimball, K.; Song, J.; Zhu, H.; Hofman, E.; Zheng, W.; Rubenstein, B. M.; Chen, O. Synthesis of All-Inorganic Cd-Doped $CsPbCl_3$ Perovskite Nanocrystals with Dual-Wavelength Emission. *J. Phys. Chem. Lett.* **2018**, *9*, 7079−7084.
(41) Ito, H.; Takano, T.; Kuroda, T.; Minami, F.; Akinaga, H. Two-Dimensional Confinement Effect on Mn^{2+} Intraionic Transition. *J. Lumin.* **1997**, *72−74*, 342−343.
(42) Majher, J. D.; Gray, M. B.; Strom, T. A.; Woodward, P. M. $Cs_2NaBiCl_6$:Mn^{2+}—A New Orange-Red Halide Double Perovskite Phosphor. *Chem. Mater.* **2019**, *31*, 1738−1744.
(43) Hu, M.; Luo, J.; Li, S.; Liu, J.; Li, J.; Tan, Z.; Niu, G.; Wang, Z.; Tang, J. Broadband Emission of Double Perovskite $Cs_2Na_{0.4}Ag_{0.6}In_{0.995}Bi_{0.005}Cl_6$:$Mn^{2+}$ for Single-Phosphor White-Light-Emitting Diodes. *Opt. Lett.* **2019**, *44*, 4757−4760.
(44) Su, B.; Zhou, G.; Huang, J.; Song, E.; Nag, A.; Xia, Z. Mn^{2+}-Doped Metal Halide Perovskites: Structure, Photoluminescence, and Application. *Laser Photonics Rev.* **2021**, *15*, 2000334.
(45) Zhang, R.; Wang, Z.; Xu, X.; Mao, X.; Xiong, J.; Yang, Y.; Han, K. All-Inorganic Rare-Earth Halide Double Perovskite Single Crystals with Highly Efficient Photoluminescence. *Adv. Opt. Mater.* **2021**, *9*, 2100689.
(46) Su, B.; Li, M.; Song, E.; Xia, Z. Sb^{3+}-Doping in Cesium Zinc Halides Single Crystals Enabling High-Efficiency Near-Infrared Emission. *Adv. Funct. Mater.* **2021**, *31*, 2105316.
(47) Yuan, X.; Zheng, J.; Zeng, R.; Jing, P.; Ji, W.; Zhao, J.; Yang, W.; Li, H. Thermal Stability of Mn^{2+} Ion Luminescence in Mn-doped Core-Shell Quantum Dots. *Nanoscale* **2014**, *6*, 300−307.

https://doi.org/10.1021/acsami.2c13878
ACS Appl. Mater. Interfaces 2022, 14, 45725−45733

(48) Yuan, X.; Ji, S.; De Siena, M. C.; Fei, L.; Zhao, Z.; Wang, Y.; Li, H.; Zhao, J.; Gamelin, D. R. Photoluminescence Temperature Dependence, Dynamics, and Quantum Efficiencies in Mn^{2+}-Doped $CsPbCl_3$ Perovskite Nanocrystals with Varied Dopant Concentration. *Chem. Mater.* **2017**, *29*, 8003−8011.
(49) Zhou, G.; Liu, Z.; Molokeev, M. S.; Xiao, Z.; Xia, Z.; Zhang, X. Manipulation of Cl/Br Transmutation in Zero-Dimensional Mn^{2+}-Based Metal Halides toward Tunable Photoluminescence and Thermal Quenching Behaviors. *J. Mater. Chem. C* **2021**, *9*, 2047−2053.
(50) Luo, B.; Guo, Y.; Li, X.; Xiao, Y.; Huang, X.; Zhang, J. Z. Efficient Trap-Mediated Mn^{2+} Dopant Emission in Two Dimensional Single-Layered Perovskite $(CH_3CH_2NH_3)_2PbBr_4$. *J. Phys. Chem. C* **2019**, *123*, 14239−14245.
(51) Wei, J.; Liao, J.; Wang, X.; Zhou, L.; Jiang, Y.; Kuang, D. All-Inorganic Lead-Free Heterometallic $Cs_4MnBi_2Cl_{12}$ Perovskite Single Crystal with Highly Efficient Orange Emission. *Matter* **2020**, *3*, 892−903.
(52) Pinchetti, V.; Anand, A.; Akkerman, Q. A.; Sciacca, D.; Lorenzon, M.; Meinardi, F.; Fanciulli, M.; Manna, L.; Brovelli, S. Trap-Mediated Two-Step Sensitization of Manganese Dopants in Perovskite Nanocrystals. *ACS Energy Lett.* **2019**, *4*, 85−93.

https://doi.org/10.1021/acsami.2c13878
ACS Appl. Mater. Interfaces 2022, 14, 45725−45733